Ultrasonics 92 (2019) 35–49

Contents lists available at ScienceDirect

Ultrasonics

journal homepage: www.elsevier.com/locate/ultras

Characterization of piezoelectric wafer active sensor for acoustic emission sensing

Yeasin Bhuiyan*, Bin Lin, Victor Giurgiutiu

Department of Mechanical Engineering, University of South Carolina, Columbia, USA

ARTICLE INFO

Keywords:
Structural health monitoring
Wave propagation
Acoustic emission sensor
Smart structures
Acoustic emission waveform

ABSTRACT

In this article, a new avenue of using the piezoelectric wafer active sensor (PWAS) for detecting the fatigue crack generated acoustic emission (AE) signals is presented. In-situ AE-fatigue experiments were conducted using PWAS along with two commercially available AE sensors. It has been shown that the PWAS and existing AE sensors successfully captured the AE signals from the fatigue crack growth in a thin aerospace specimen. Two experiments were conducted using the PWAS with each of the commercial AE sensors. For each experiment, two AE analyses were performed: (1) the hit-based analysis, (2) the waveform-based analysis. The fatigue loading was synchronized with the AE measurements. This allowed comparing the AE hits due to a particular AE event captured by PWAS and the other sensors. All the sensors showed a very similar pattern of AE hits as observed from the hit-based analysis. The AE waveform-based analysis was used to compare the waveforms and their frequency spectra captured by the three sensors. The commercial PICO showed ringing in the AE signals and showed a weak response in high-frequency region. The commercial S9225 had better signal-to-noise ratio but it also showed a weak response in high-frequency region. It was found that all sensors captured the low-frequency flexural modes of the guided acoustic waves. However, the high-frequency acoustic wave signals were predominately captured by the PWAS. The AE waveform-based analysis provided more insight of the AE source and guided wave propagation modes.

1. Introduction

To develop a comprehensive understanding of the physics of the acoustic emission (AE) sources, a better and reliable sensor is the key component for the AE detection. The acoustic emission technique had been used for a wide range of applications for the structural health monitoring (SHM) and non-destructive evaluation (NDE) [1–4]. The acoustic emissions from the fatigue crack had always been of an interest to the researchers [5–9].

One of the major challenges of the fatigue crack-related acoustic emissions is that a simple fatigue experiment could generate a huge amount of AE data which could make it difficult to analyze the individual AE waveform [10,11]. Most of the researchers focused on analyzing the gross parameters such as AE hits, total energy, count rate, cumulative AE hits [12]. But the acoustic emission waveforms contain a wealth of information regarding the online damage occurrence in the structures [13,14]. The fatigue crack length extraction by analyzing the AE waveforms had been attempted [15,16]. The fatigue crack from the thin specimen generates various groups of AE signals [17]. Each group has a specific amplitude level and frequency spectrum.

Various types of AE sensors were used to capture the acoustic emissions [18–22]. Piezoceramic-based AE sensors were very popular and commercially available to measure the acoustic emissions [23–25]. However, these piezoceramic AE sensors were mostly sensitive to the flexural wave motion (vertical motion to the surface) [23,26]. The acoustic emissions due to impact hammering, fatal failure, large disturbances, glass fracture had a high-amplitude vertical (out-of-plane) component of wave motion and these AE sensors were also well-constructed to sense these wave motion [27–32]. Guided ultrasonic imaging approach [33] and surface response to excitation (sure) method [34] have been used for defect detection and quantification. Attempts were made to capture the in-plane component of the wave motion using fiber-Bragg grating sensors [35–37]. However, the optical noise of the photodetector prohibited to capture the low-amplitude AE signals.

Coupled piezoelectric film strain sensors, monolithic piezoceramic patches were used to measure the acoustic waves [38,39]. The partial discharge acoustic emission array sensors and SE150M type sensor were used for detecting crystal dislocation generated AE signals [40,41]. AE hits from a notched crack in a thick specimen were captured by the piezoelectric AE sensors [42]. The surface waves were dominant in the

---

* Corresponding author.
E-mail address: yeasin85@gmail.com (Y. Bhuiyan).

https://doi.org/10.1016/j.ultras.2018.08.020
Received 1 August 2017; Received in revised form 30 August 2018; Accepted 31 August 2018

thick specimen. The AE signals due to the fatigue cracks are much more complex than the simple pencil lead break (PLB) and impact damage [12,43–46]. Three types of elastic waves were obtained during a fatigue test in the aluminum specimen [47]. AE signals from the fatigue damage in a round steel specimen were analyzed by Amer et al. [48]. They showed three clusters of elastic waveforms, one of which had very low energy content as compared to the other two. However, none of them showed exactly at what load level the acoustic emissions could happen from the fatigue-crack.

Piezoelectric wafer active sensors (PWAS) were commonly used for detecting plate guided waves [49]. Preliminary work had been performed to capture the PLB (pencil lead break) generated AE and some fatigue AE hits from steel specimen in our research group [50]. However, the detail characterization was not investigated with AE waveform based analysis and fatigue load synchronization. A network of piezoelectric sensors was used for fatigue-crack evaluation using nonlinear ultrasonic waves [51]. It had been shown that they successfully captured the ultrasonic guided waves in active detection technique. However, in an active detection method, a user-defined excitation signal can be chosen until a sufficiently high amplitude signal is obtained in the sensor [52]. These sensors were also used for energy harvesting applications [53]. The potential advantage of using the PWAS transducer would be that it could measure both symmetric (in-plane) and antisymmetric (out-of-plane) guided wave motion through the in-plane strain sensing mechanism. The suitability of the PWAS transducers in application to fatigue-crack generated AE signals are yet to be analyzed.

The novelty of the article is that the PWAS has been used to capture the fatigue-crack generated acoustic emission signals. First, the PWAS was tested with S9225 AE sensor by conducting an in-situ AE-fatigue experiment. The comparison of the two results is discussed based on the AE hit based and waveform based analysis. Then, the PWAS was tested with PICO AE sensor by conducting a similar experiment on the same specimen. Similar comparison studies were performed. It has been shown that PWAS successfully captured the AE signals and gave a better signal-to-noise in the high-frequency region than the commercially available AE sensors (S9225 and PICO).

2. Sensor selection

In this research, a thin plate-like specimen with 1-mm thickness was used. The total mass of the specimen was only 82 g. Intuitively, a sensor has to be lighter than the specimen. Past experiments and multiphysics simulations showed that the size and mass of the sensor tremendously affect the local wavefield proximate to the sensors [15,54]. Based on the literature survey [8,12,22,55], manufacturer guidelines [56], and our previous studies, following criteria were set to choose the sensor for this application:

1. Lightweight and smaller size sensor to minimize the interference between the sensor and true wavefield in the structure
2. Wide frequency band to pick up a wide range of frequencies

All the three sensors (S9225, PICO and PWAS) used in this research meet these criteria. According to the manufacturer, the two sensors (model: S9225 and PICO) were the miniature type, lightweight, and have wideband frequency responses. Masses of both sensors are less than 0.5 g. PICO and S9225 are suitable for wideband frequency application up to 750 kHz and 1500 kHz [56]. Specifically, when the exact frequency contents of desired AE signals are not known (as in this case), the wideband frequency band sensors are usually suggested. These sensors are the leading edge products that are commercially available. There are some other wideband sensors (for example, model: WSα, nano-30 from PAC Mistras) that has been tested before. However, they are relatively heavy weight sensor and may modify the local wavefield.

PWAS used in this research was lightweight (mass 0.15 g) and smaller size (7 mm diameter, 0.5 mm thickness). This size of PWAS was selected to cover a wide range of frequencies. The frequency response curve of PWAS depends on the PWAS size, sensing mode, and thickness of the host structure. The frequency response of the selected PWAS bonded to the structure is shown in Fig. 1. The bandwidth should be such that it could cover the entire frequency spectrum of the AE signals. The authors would prefer to have some calm and stable response in the frequency domain to ensure that it has covered the entire frequency spectrum.

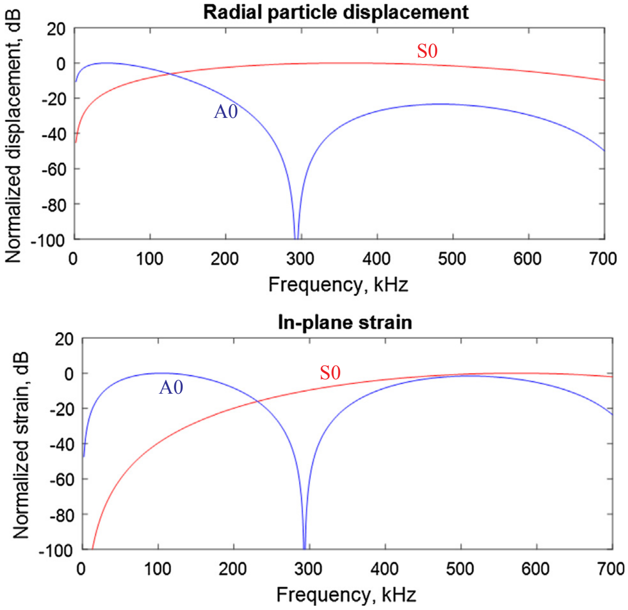

Fig. 1. PWAS frequency response plot in dB scale: (a) for radial displacement, (b) for in-plane strain measurement (obtained using analytical expressions given in Ref. [57]).

The thickness of PWAS affects the sensing of acoustic waves. In general, the output sensing voltage is linearly proportional to the PWAS thickness. The mathematical relation between the PWAS thickness and voltage sensing is given by Eq. (1) [57].

$$V = t\frac{k_{31}^2}{(1-k_{31}^2)}\frac{1}{d_{31}}S_1 \tag{1}$$

where t is the PWAS thickness, K_{31} is electromechanical coupling coefficient, d_{31} is piezoelectric charge constant, S_1 is the in-plane strain. The values of the constants are given in Table 1. Following Eq. (1), the higher thickness of PWAS is desirable, but it adds up more weight on the specimen. Thus, output voltage and weight of PWAS. We found that 0.5-mm thick PWAS could generate enough voltage to sense the acoustic strain wave in this application.

Table 1
Material properties of PZT in PWAS [58] (relevant to d_{31} operation mode).

Material properties	Symbol	Value
Electromechanical coupling coefficient	K_p	0.63
	K_{31}	0.35
Piezoelectric charge constant	d_{31}	-190×10^{-12} m/V
Piezoelectric voltage constant	g_{31}	-12.6×10^{-3} Vm/N
Elastic Constant (Young's modulus)	Y_{33}	56 GPa
	Y_{31}	76 GPa
Dielectric permittivity	ε_{33}	1850 ε_0 @1 kHz $\varepsilon_0 = 8.854 \times 10^{-12}$F/m
Dissipation factor	tanδ	1.2% @1 kHz
Curie temperature	θ	320 °C
Density	ρ	7800 kg/m^3

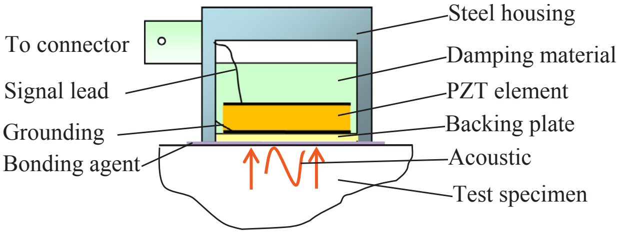

Fig. 2. Cross-section of a typical commercial AE sensor. It measures out-of-plane wave motion.

3. Fabrication and operating principle of the sensors

3.1. Commercial AE sensors

The schematic of the cross-section of a typical commercial AE sensor is shown in Fig. 2. It has several components inside a steel housing. It has a backing plate, PZT material, electrodes, and damping material inside the housing. The top electrode of the PZT material is connected to the center conductor of the connector and the bottom electrode is grounded to the housing. A bonding agent is used to bond the AE sensor to the host structure.

In general, the commercial AE sensors (e.g. S9225 and PICO) measures the pressure applied on the surface of the sensor due to the acceleration of the surface particle of the specimen [21]. Piezoelectric elements inside the sensor convert this pressure into current, which then converted to a voltage signal for measurement [21]. These transducers are sensitive to vertical motion aka out-of-plane motion of the particle due to the acoustic wave propagation in the specimen [18]. The output from these sensors is proportional to the normal displacement of the particle [8]. The detailed constructional information and properties of the inside elements are proprietary information.

3.2. PWAS transducers

PWAS transducers are small, lightweight, inexpensive, and can be produced in different geometries [57]. They can be permanently bonded on host structures in large quantities and achieve real-time monitoring of the structural health status. They can be conveniently used for transmitting and receiving guided waves. A PWAS mounted on a structure is shown in Fig. 3a.

The sensing mechanism of a PWAS is illustrated in Fig. 3b. It can measure both symmetric (wave motions are predominantly in-plane) and antisymmetric Lamb wave modes (wave motions are predominantly out-of-plane) [54]. PWAS transducers couple the electrical and mechanical effects (mechanical strain, S_{ij}, mechanical stress, T_{kl}, electrical field, E_k, and electrical displacement, D_j). The piezoelectric constitutive equations in tensor notations can be written as

$$\begin{aligned} S_{ij} &= s^{E}_{ijkl} T_{kl} + d_{kij} E_k \\ D_j &= d_{klj} T_{kl} + \varepsilon^{T}_{jk} E_k \end{aligned} \tag{2}$$

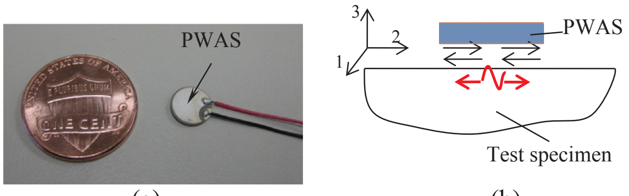

(a) (b)

Fig. 3. (a) A piezoelectric wafer active sensor (PWAS), (b) PWAS sensing mechanism: it measures in-plane and out-of-plane wave motion through in-plane strain sensing [54]. 1, 2, 3 indicates three perpendicular directions (3 direction is along the thickness of PWAS).

where s^{E}_{ijkl} is the mechanical compliance of the material measured at zero electric field ($E = 0$), ε^{T}_{jk} is the dielectric permittivity measured at zero mechanical stress ($T = 0$), and d_{klj} is the piezoelectric coupling effect. The coupling effect d_{klj} represents polarization generated per unit of mechanical stress (T_{kl}) applied to a piezoelectric material or, alternatively, the mechanical strain (S_{ij}) experienced by a piezoelectric material per unit of electric field applied. The coupling depends on the polarization of the lead zirconate titanate (PZT) element during the manufacturing process. In principle, they can be polarized in many directions depending on applications but the thickness-wise polarized PWAS has been used in this research.

In this research, PWAS utilized d_{31} operation mode, where 3 is along the thickness direction and 1 is along the in-plane radius direction. The reason for choosing this type of operation mode was to measure in-plane strains, S_1, S_2 by generating a transverse electric voltage signal (E_3). The relevant (to d_{31} operation mode) material properties of PZT element in PWAS are listed in Table 1.

4. AE-Fatigue experiment with PWAS and S9225 sensors

An in-situ AE-fatigue experiment was designed to measure the AE signals from the fatigue crack growth under application of axial cyclic fatigue loading. A commonly used material for fatigue-prone components of the aircraft, aluminum Al-2024T3, was used to make the test specimen. A thin plate-like specimen was manufactured. The dimension of the specimen was 305 mm (12 in.) in length, 100 mm (4 in.) in width, and 1 mm (0.04 in.) in thickness.

The schematic diagram of the experimental setup is shown in Fig. 4. A small (1-mm diameter) hole was drilled at the center of the specimen to initiate the crack and a 20-mm pre-crack was created under cyclic fatigue loading. The test specimen was then equipped with a PWAS transducer. A commercially available AE sensor (model S9225 from PAC MISTRAS Inc.) was also bonded symmetrically to the crack. The sensors were bonded at 5-mm from the fatigue crack (the fatigue crack was centered in the specimen). A strain gauge was also bonded at 40-mm from the crack that provided with the fatigue loading information directly from the specimen.

Such proximity of the two sensors from the crack would allow

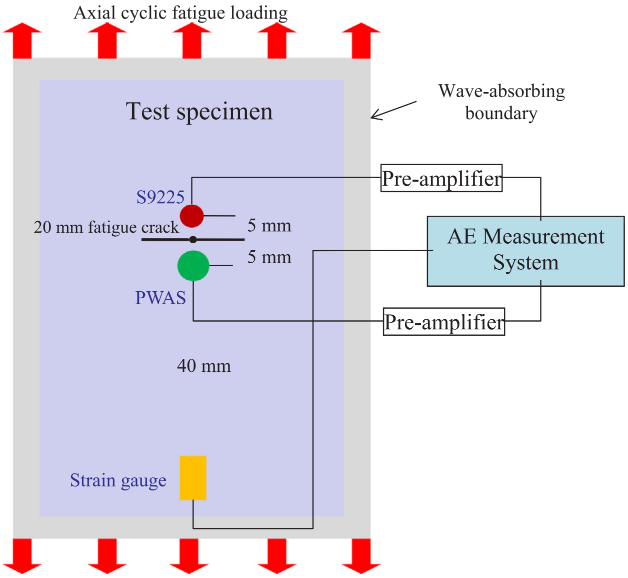

Fig. 4. Schematic diagram of the experimental setup. The specimen was under axial cyclic fatigue loading to cause the crack growth. PWAS transducer and S9225 AE sensor were symmetrically bonded at 5-mm from the crack and captured the acoustic emissions from the fatigue crack; strain gauge was bonded 40-mm from the crack to obtain the load information directly from the specimen.

capturing low-amplitude AE signals which would otherwise diminish due to geometric spreading and any material damping as they travel away from the crack. A wave absorbing clay boundary was also used around the edges of the plate. It would prevent the AE signals from being contaminated by the reflected wave signals from the plate edges. It would also resemble an actual large structural part of the aircraft where the reflected waves from the edges would diminish before reaches to the sensors.

Both sensors were connected with identical preamplifiers. The preamplifiers were coming with the AE system and had a built-in band-pass filter (30–700 kHz). A 40 dB gain was selected for both pre-amplifiers. Thresholds of the two sensors were selected just above the environmental noise level. For PWAS, the threshold was set to 2 dB above its noise level (51 dB). For S9225, the threshold was set to 2 dB above its noise level (38 dB). In terms of noise level, PWAS seems to have more electromagnetic noise. There are ways to denoise the PWAS waveforms as discussed in Section 4.4. Also, it was observed from the experimental results that the collected signal was much stronger than the noise floor. Some AE signals were so strong that the signal to noise ratio (SNR) was very high (shown later). Some signals have relatively low SNR, and in that case, the effect of noise can be minimized by adopting a proper signal processing method. A relatively higher sampling rate (10 MHz) was chosen to capture any high-frequency AE signals.

A hydraulic MTS machine was used to apply the fatigue loading to the instrumented specimen. A specimen mounted on the MTS grip is shown in Fig. 5a. The close-up views of the two sensors are shown in Fig. 5b and c. An axial tensile cyclic fatigue loading was sinusoidally varied between a maximum and minimum load level maintaining an R-ratio ($\sigma_{\min}/\sigma_{\max}$) of 0.1. The maximum load level ($F_{\max}$) was 12.3 kN and the minimum load level ($F_{\min}$) was 1.23 kN. The slow loading rate (0.05 Hz) was used to avoid any interference of the loading frequency with the AE signal frequencies. The band-pass filter was used to filter out any low or high-frequency noise from the mechanical interferences such as MTS grips, friction between the wave absorbing clay boundary and test specimen.

Three parallel systems were used simultaneously during the AE-fatigue experiment: (a) fatigue loading by the MTS machine, (b) AE and fatigue loading measurement by the AE system, and (c) fatigue crack growth measurement by a high-resolution (1280 × 964 pixels and 3.75-µm each pixel size) video recorder (Fig. 6). Since the AE measurement and the load recording was performed in the same AE measuring system, it allowed better synchronization between the load and AE measurement. Thus, the acoustic emissions and the fatigue loading had a common timeline.

The crack growth was optically measured by using proper light source and lens with various extension tubes. These extension tubes provide different zoom levels as illustrated in Fig. 7. The crack tip was monitored with the highest zoom level to properly monitor the crack growth. A scaled tape was attached next to the crack to easily track the crack length.

4.1. Similarity between PWAS vs S9225

The AE hit-based analysis shows a similar pattern in PWAS and S9225 results. The AE hits were captured by the PWAS and S9225 AE sensors as the fatigue crack grew. A source localization method was performed to verify that fatigue crack was the source of these AE hits and reported in our recent communication [17]. Hence, the source localization is not repeated for the sake of brevity. The AE hits captured by the PWAS and S9225 for 60 fatigue cycles are shown in Fig. 8a and b. In this particular 60 fatigue cycles, crack growth was optically measured as 300-µm. The average crack growth can be calculated as 5-µm/cycle. This section of the AE recording contained a jump (transition) of AE hits. The transition can be noticed at around 550 s in Fig. 8.

Both AE hit plots show a similar pattern in the hit-amplitude

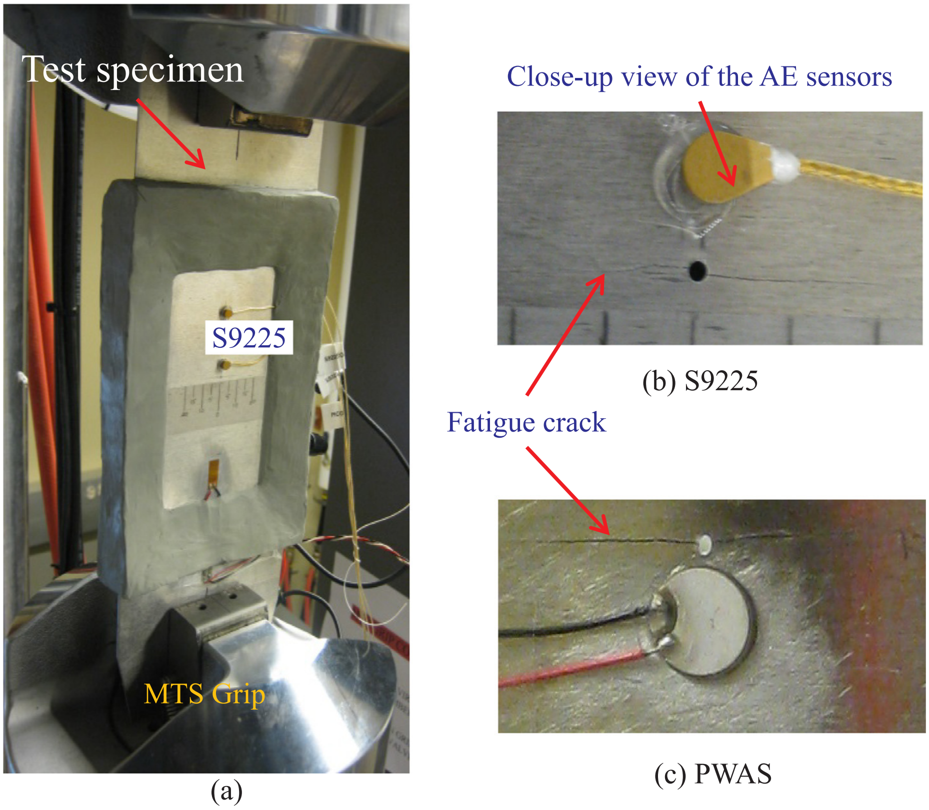

Fig. 5. (a) Experimented test specimen subjected to fatigue loading on MTS load frame, close-up view of the AE sensors: (b) S9225 AE sensor bonded to the one side of the specimen and (c) PWAS transducer bonded to the other side of the specimen. [for scale, please note the hole has 1-mm diameter]

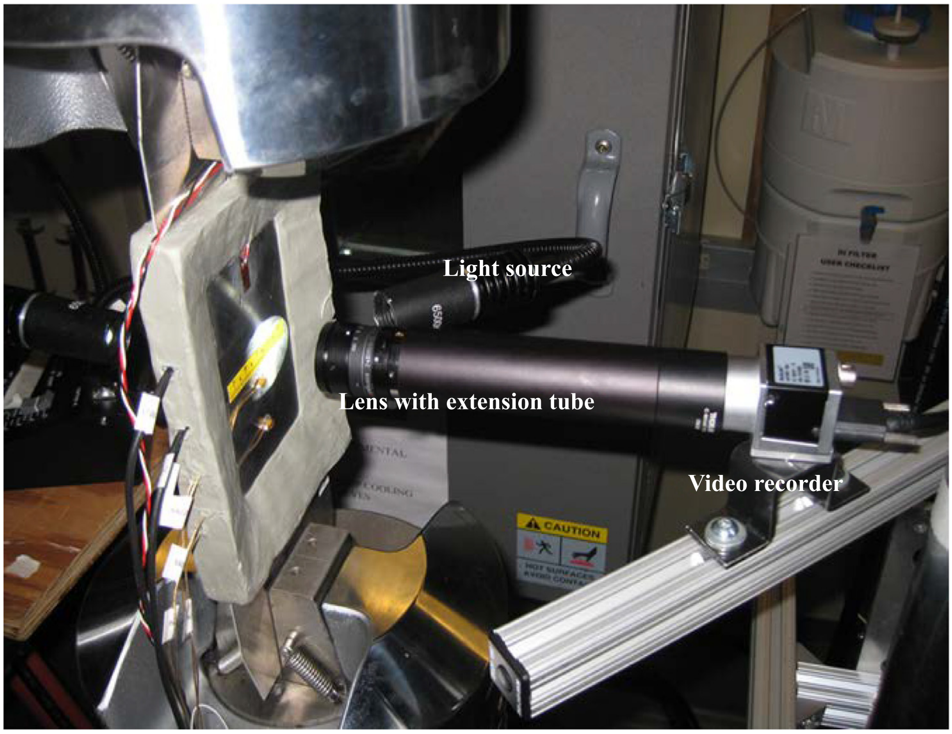

Fig. 6. Optical setup for the crack growth measurement. A proper light source was used to illuminate the crack from the front and back. A high-resolution video recorder and lens with extension tube were used to optically monitor the crack.

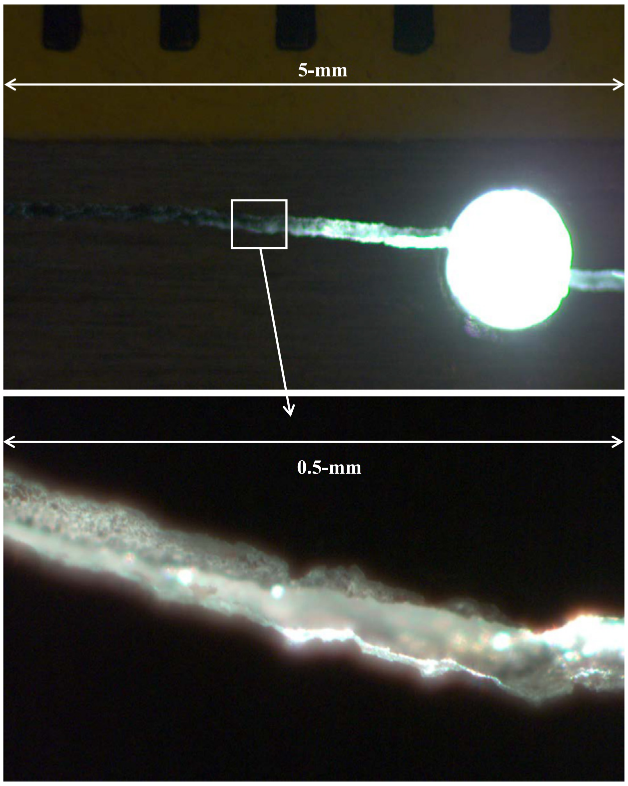

Fig. 7. Fatigue crack was shone from the back. Two different zoom levels (field of view, FOV: 5 × 3 mm^2 and FOV: 0.5 × 0.3 mm^2) of the lens to properly monitor the crack. The latter zoom level was used to monitor the crack tip extension.

variation as illustrated in Fig. 8. The hit-amplitude corresponds to the maximum amplitude of an AE waveform converted into a decibel (dB) scale. It can be observed from the PWAS AE-hit plot (Fig. 8a) that there are lower-amplitude AE hits. Most of them had an almost constant amplitude of 70 dB with some variations below and above the 70 dB. Similarly, S9225 captured these AE hits (Fig. 8b). Most of them had an almost constant amplitude of 45 dB with some variations below and above the 45 dB. Both PWAS and S9225 captured the new AE hits happened after 550 s. The new AE hits had higher amplitudes than the previous AE hits and the amplitudes were almost constant with a little variation.

These new AE hits have about 96 dB hit amplitudes in the PWAS AE hit plot (Fig. 8a) and about 67 dB hit amplitudes in the S9225 AE hit plot (Fig. 8b). The PWAS hit amplitudes were higher than that of the S9225. This may be because the size of the PWAS transducer (7 mm diameter) was larger than the size (3.5 mm diameter) of the S9225 AE sensor. Also, they had different piezoelectric transduction factors, and sensing mechanisms. It can also be noticed that PWAS captured 167 AE hits while the S9225 captured 134 AE hits because some of the low-amplitude AE hits fall below the threshold setting of S9225. Except these very low-amplitude AE hits, both of them successfully captured the fatigue crack generated AE events.

The fatigue loading information was captured directly from the specimen by the bonded strain gauge. Since the AE measurements and the load recording were performed by using the same AE machine, the PWAS AE hits, S9225 AE hits and the fatigue loading shared a common timeline. This allowed us to know exactly at what load level the AE hits had happened. The overall view of AE hits synchronized with the fatigue loading cycle is plotted in Fig. 9. The AE hit amplitudes are scaled in such a way that the AE hits of PWAS and S9225 can show the one-to-one correspondence, together with cyclic load variation. The maximum PWAS AE hit amplitude is scaled to unity and all the other PWAS AE hits are divided by that maximum value. Similarly, the maximum S9225 AE hit amplitude is scaled to unity and all the other S9225 AE hits are divided by that maximum value. By using this kind of scaling, we are able to merge two plots of Fig. 8 into a single plot in Fig. 9

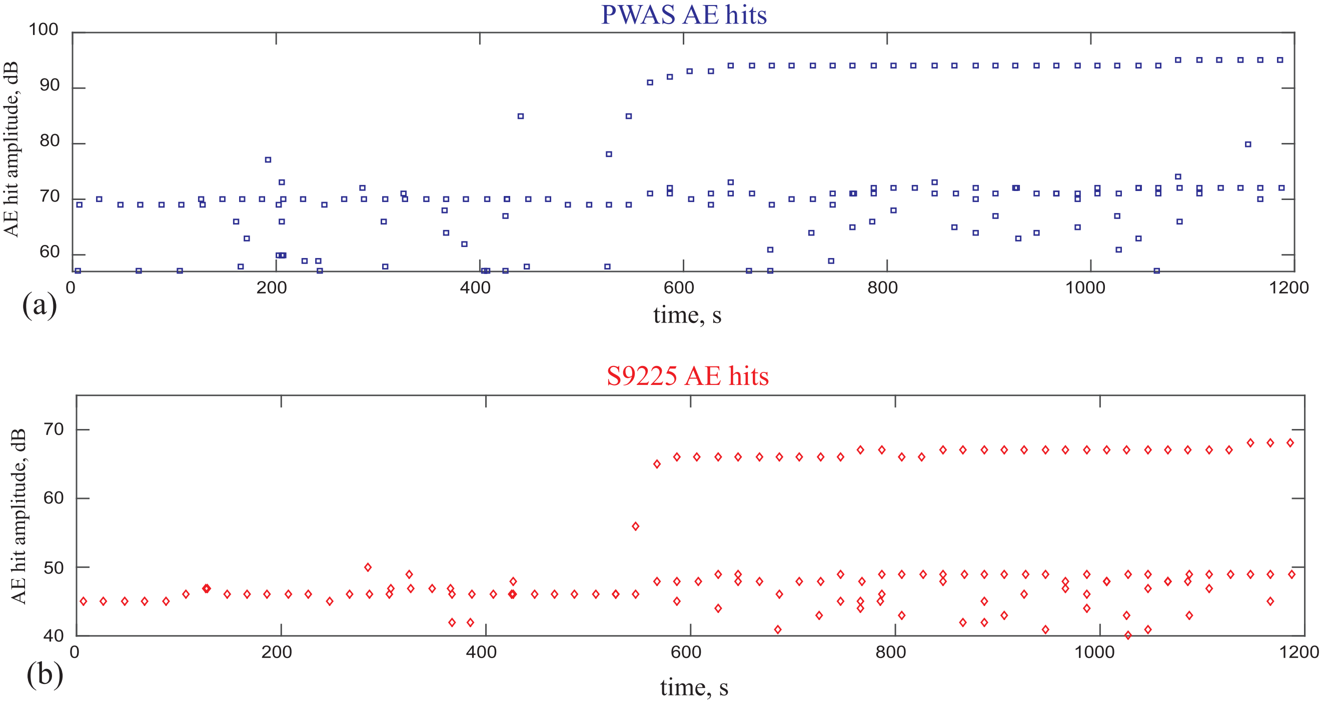

Fig. 8. AE hits captured by (a) PWAS and (b) S9225 AE sensors, both of them showing the similar trend in the AE-hit plot. A jump (transition) in the AE hit was observed near 550 s in both plots. In these plots, PWAS has 167 hits and S9225 has 134 hits.

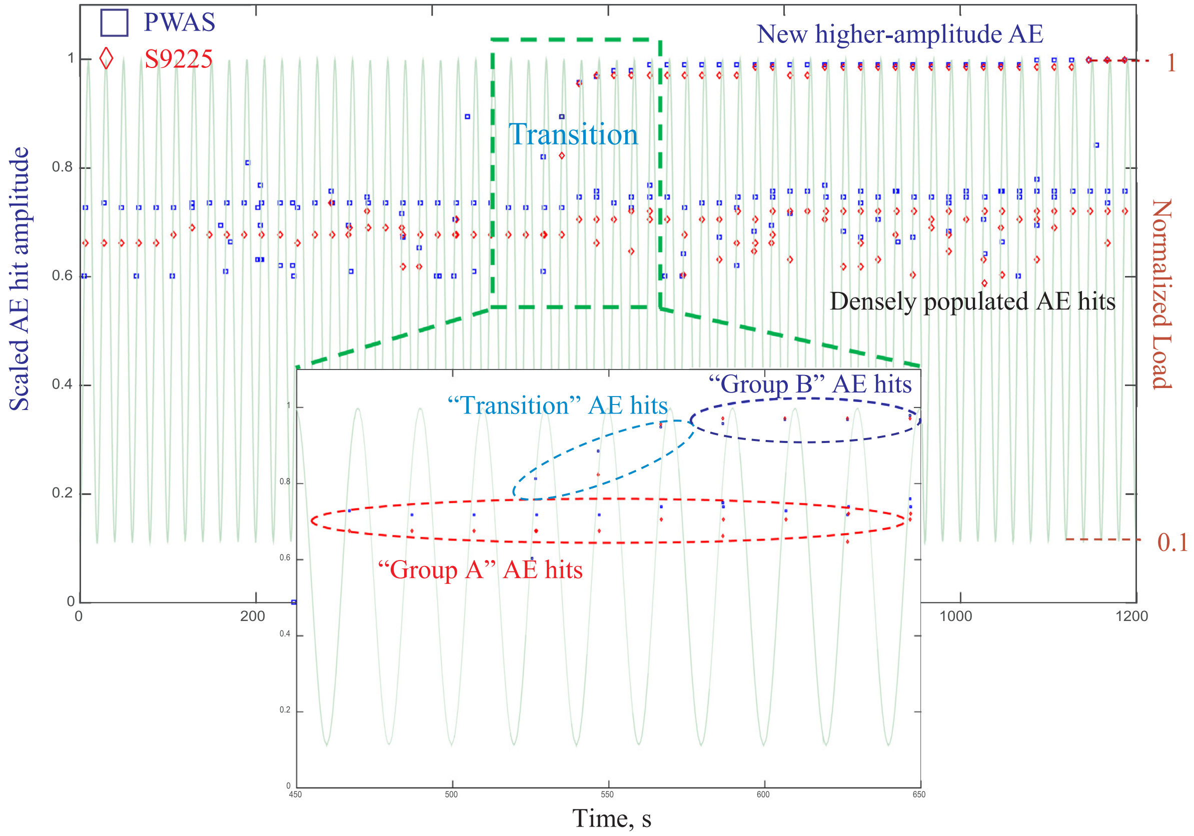

Fig. 9. The overall view of AE hits synchronized with the fatigue loading cycle (Fmax = 12.3 kN, Fmin = 1.23 kN). The AE-hits are scaled in such a way that they could show the one-to-one correspondence. Inset Figure shows the zoomed in view of the transitioning of the AE hits. The densely populated AE-hits had relatively lower amplitudes and there are new higher amplitude AE-hits after the transition period.

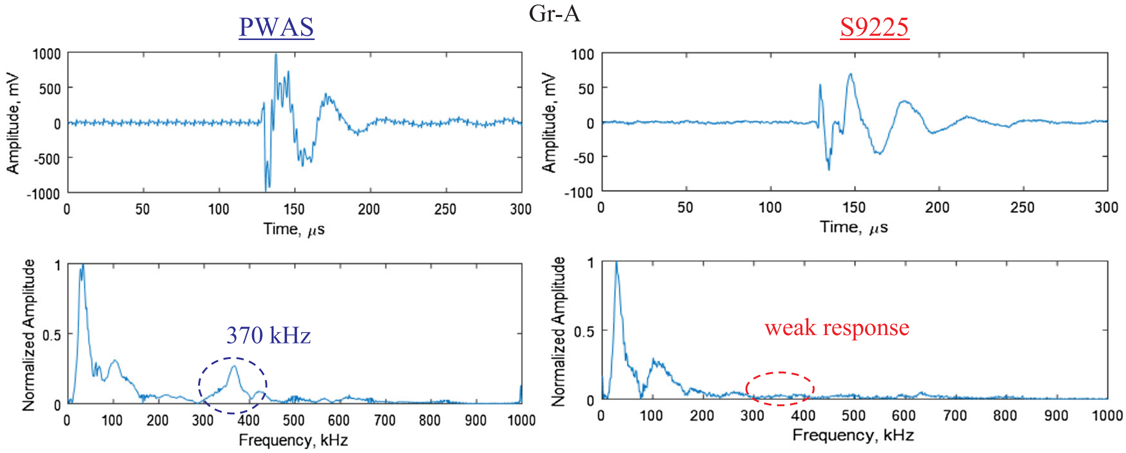

(a)

(b)

Fig. 10. The “group A” AE waveform and its frequency spectrum for the same AE event captured by the PWAS and S9225 AE sensors. Both of them captured low frequencies until 170-kHz. The PWAS captured low-frequency contents plus a 370-kHz frequency peak.

without any alteration. The two AE hit plots of Fig. 9 share the same scaled AE hit amplitude indicated by the left bar and of course, the actual values can be obtained using Fig. 8.

The cyclic loads are normalized by the maximum load level and overlapped with the AE hit plots. The right bar indicates the normalized load information. We would be able to show all the three plots together in a single Fig. 9 by using the combination of the scaling and normalizing process mentioned above. AE hits happened at every cycle as shown in Fig. 9. PWAS and S9225 AE hits are seemed to be in sync. From the overall view, the two groups of AE hits can be immediately identified: densely populated AE hits (Group A) and new higher-amplitude AE hits (Group B) as labeled in Fig. 9. The densely populated AE hits persisted along with the higher-amplitude AE hits.

The inset of Fig. 9 clearly shows the AE hits of PWAS and S9225 with the cyclic loading. At a particular time, a pair of AE hits can be observed: one captured by PWAS (marked by blue “square”), other captured by S9225 (marked by red “diamond”). This indicated that they captured the same AE event at almost same time. The AE hits occurred during the cyclic loading period (from minimum load to maximum load) only. In the unloading period (from maximum load to minimum load), no AE hits were observed.

The transition AE hits as shown in the inset of Fig. 9 may be responsible for a change in the fatigue crack growth mechanism. As it was noticed from the optical crack growth measurement that the fatigue crack grew relatively faster after this transition AE hits. The crack growth was optically measured by using a high-resolution video recorder and a tape with measuring scale was bonded next to the fatigue crack (as seen from Fig. 5). Although the optical measurement was not the focus of this research, it helped for AE signal interpretation.

The PWAS and S9225 showed very similar pattern so far based on the AE-hit analysis. Both of them captured the fatigue crack generated AE hits with the very similar level of detail. The hit-based analysis only considers the “maximum amplitude” of the AE signal. The waveform-based analysis considers of the maximum amplitude, time domain pattern, and the frequency spectra of the AE signals. Thus, the AE waveform-based analysis may help to understand more about the evolution of different AE hits. In addition, the frequency spectra of the AE signals may give information about the fatigue crack growth mechanism explanation. We have recently shown that the frequency spectra of the AE waveforms allowed multiple groupings of the AE signals and each group represents a particular fatigue crack growth mechanism [17].

There are three different AE hits (group A, group B, and transition) as shown in Fig. 9. They have different levels of amplitude as well as frequency spectra. The frequency spectra are detailed in the next section. These AE hits may be related to the fatigue crack growth mechanism. Group A and B both AE hits were observed in every fatigue cycle after the transition. There may be several micro-fracture events happening at the crack tip which may result in several AE hits. These fracture events may be related to the material grain structures. Due to various size and shape of the grain structures, the fracture events may be quite different which may produce these AE hit groups. Before the transition, there may be a particular type of fracture events which may cause only group A AE hits but after the transition, there may be another fracture event added to the previous type of fracture event which may result in group B along with group A AE hits. This added fracture events may eventually dictate the fatigue crack growth. Also, the group B happened at relatively lower load (78%F_{max}) but higher amplitude than group A which happened at higher load (84%F_{max}) but lower amplitude. Please note that the load level for each AE hit was obtained by drawing a vertical line from the hit to the cyclic loading line (the vertical line is not shown in Fig. 9). It means that in the cyclic fatigue loading, when the load kept increasing (ramping up) the group B AE hit occurred earlier than the group A. It indicates that the first fracture event released higher amplitude than the subsequent fracture event.

4.2. AE waveform-based analysis for PWAS and S9225 results

The waveform-based analysis was performed to further compare the PWAS and S9225 AE sensors. Each AE hit corresponded to an AE waveform. The Fast Fourier Transform (FFT) of the time-domain waveform was performed to obtain the frequency spectrum of the waveform. It was found that all the PWAS AE hits in the densely populated region (Fig. 9) had almost similar waveforms and the frequency spectra. Also, all the higher-amplitude AE hits (Fig. 9) had the similar waveform and frequency spectra. The similar observation can be made for the S9225 AE hits. But, some differences were observed in the PWAS and S9225 AE waveforms.

A representative waveform from the densely populated region (group A) was chosen for comparison. The PWAS and S9225 AE waveforms for a particular AE event are shown in Fig. 10. Both time-domain waveform and frequency spectra were illustrated in Fig. 10. It shows that the low-frequency peaks at 40 and 100 kHz are successfully captured by both PWAS and S9225 AE sensors. But, the PWAS transducer captured a 370-kHz frequency peak that was somehow weaker in the frequency spectrum of S9225. Group A waveforms happened at 84% of the maximum load level which was same for both PWAS and S9225.

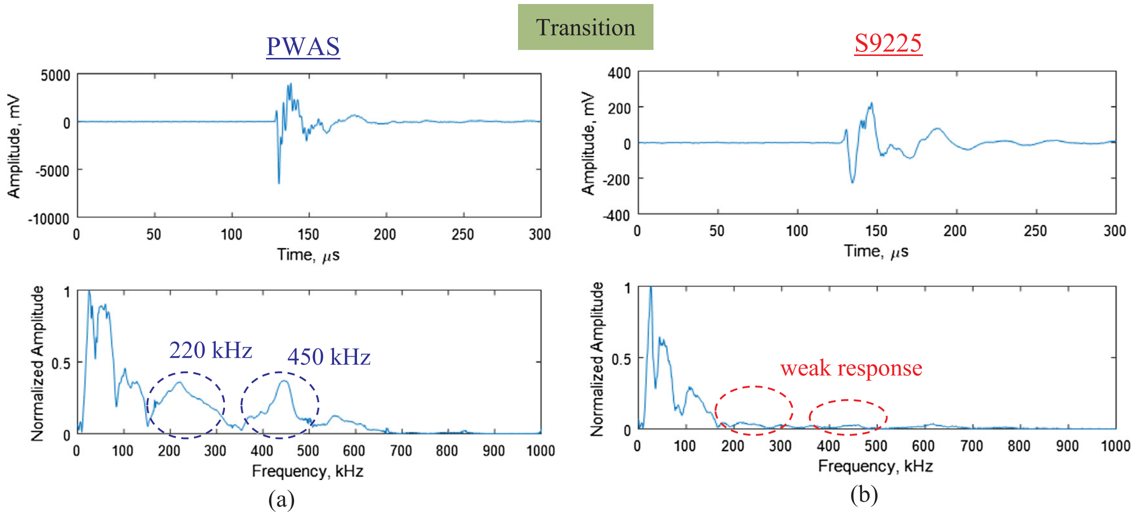

Fig. 11. The "transition" AE waveform and its frequency spectrum for the same AE event captured by the PWAS and S9225 AE sensors. Both of them captured low frequencies until 170-kHz. The PWAS captured low-frequency contents plus 220-kHz, and 450-kHz frequency peaks.

A representative waveform corresponding to the AE hits in the transition region (inset of Fig. 9) was also considered for the comparison between PWAS and S9225. The time domain waveforms and the frequency spectra of the "transition" AE waveforms captured by PWAS and S9225 are shown in Fig. 11. Both waveforms happened at the same time and corresponded to the same AE event. The peak amplitude of the transition waveform was about five times higher than that of the group A waveform which was similar for both PWAS and S9225 time-domain waveforms. The low frequencies up to 150-kHz were captured by both PWAS and S9225 AE sensors. But, the PWAS transducer captured 220-kHz and 450- kHz frequency peaks that were very weak in the frequency spectrum of S9225.

Now the higher-amplitude AE waveforms (group B) can be compared. For a particular AE event, group B time-domain waveform and frequency spectra are shown in Fig. 12. At first, the group A and group B frequency spectra of the PWAS waveforms can be compared by using Figs. 10a and 12a. The frequency spectra of group A and B AE waveform were different, as expected since they happened at different load levels. Group B happened at 78% of maximum load level (78%F_{max}) whereas group A happened at 84% of maximum load level (84%F_{max}). Group A had 40, 100, 370-kHz peaks whereas group B had 30, 60, 100, 220, 450-kHz peaks. Thus, based on PWAS waveform capture, there were significant differences between group A and B waveforms.

The group A and B frequency spectra of S9225 waveforms were compared by using Figs. 10b and 12b. It can be observed that group A had 40, 100-kHz frequency peaks and group B had 30, 60, 110-kHz frequency peaks. Thus, based on S9225 waveform capture, there was not much difference between group A and B waveforms. This is because S9225 showed a very weak response in 220-kHz and 450-kHz peak frequencies as marked by dotted ellipses.

The waveform-based analyses of the experimental results show that in general, there is a relatively stronger amplitude below 200 kHz. There are commercially available AE sensors (e.g. R15I-AST, R15α, R15, etc.) that are resonant type and specifically designed for a frequency (e.g. 150 kHz, 200 kHz). In general, they are very heavy weight sensors (for example, the mass of R15I-AST is 68 g, R15α is 35 g). They can easily modify the acoustic wavefield in the lightweight specimen. Please note, there are also higher frequencies (e.g. 370, 450 kHz) as observed in the PWAS recorded waveforms. It would be much difficult to capture the higher frequencies by using the lower frequency resonant type sensors.

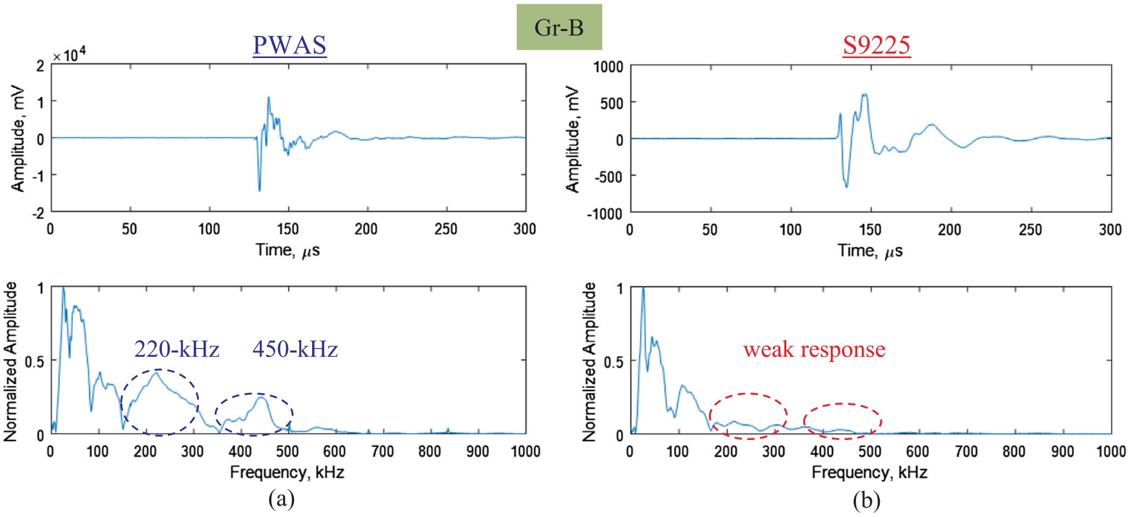

Fig. 12. The "group B" AE waveform and its frequency spectrum for the same AE event captured by the PWAS and S9225 AE sensors. Both of them captured low frequencies until 170-kHz. The PWAS captured low-frequency contents plus 220-kHz, and 450-kHz frequency peaks.

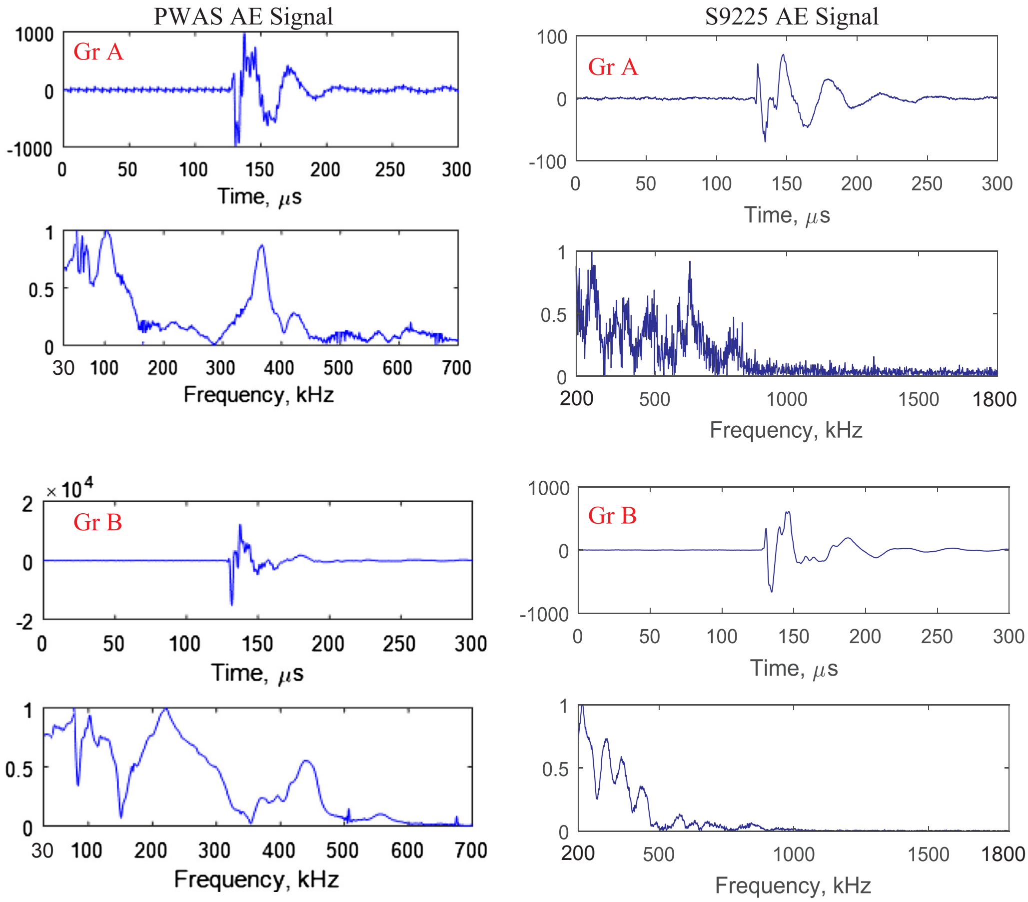

Fig. 13. Comparison of PWAS and S9225 AE waveforms and their frequency spectra within specified bandwidths (for PWAS: 30–700 kHz, for S9225: 200–1800 kHz).

4.3. AE waveform analysis for PWAS and S9225 within their specified bandwidth

It can be noticed from Fig. 10 through Fig. 12 that there is larger amplitude of the low-frequency component, especially for S9225 AE waveforms. The commercial AE sensor (S9225) is specified within 200–1800 kHz frequencies. Therefore, S9225 AE waveforms are filtered with high pass filter with a cut-off frequency of 200 kHz. Both group A and group B filtered AE signals and their frequency spectra are shown in Fig. 13. The entire frequency spectrum of the specified bandwidth of S9225 is plotted in Fig. 13.

The similar filtering was performed for PWAS AE waveforms with a cut-off frequency of 30 kHz since PWAS response curve (Fig. 1) shows that it can measure the AE signals within 30–700 kHz. The filtered frequency spectra of group A and group B waveforms of PWAS are shown in Fig. 13. PWAS frequency spectrum of group A waveform shows higher signal to noise ratio than that of S9225. PWAS response is relatively stronger in 370 kHz and 450 kHz than that of S9225. However, the frequency spectrum of S9225 for group B signal has less noise than that of group A waveform. Because, the amplitude of group B waveform is much stronger than group A waveform.

4.4. Possible explanation for weak response of S9225

The frequency response characteristic curve of S9225 was collected from the manufacturer (Fig. 14b) to find out why the S9225 AE sensor was showing a weak response at some higher frequencies (220, 370, 450-kHz). The frequency response plot (Fig. 14b) showed that S9225 had a week response in 170–300 kHz frequencies as marked by two dotted lines. On the S9225 sensing signal's frequency spectrum plot (Fig. 14a) also showed a weak response in these frequencies. This explained why S9225 was showing a weak response to the 220-kHz frequency peak.

The frequency response characteristic plot showed that S9225 was a fairly wideband sensor in the range of 350–920 kHz. But why S9925 was showing a weak response in capturing 370-kHz and 450-kHz frequency peaks?

This may be because of the sensing mechanism. As discussed earlier that the commercial AE sensors (such as S9225 and PICO) usually measures the pressure applied on the surface of the sensor due to the acceleration of the surface particle of the specimen and they are sensitive to vertical (out-of-plane) motion. Several researchers reported this before [8,18,21] and is not repeated for the sake of brevity.

On the other hand, PWAS transducers measure in-plane strain. They are sensitive to both symmetric and antisymmetric multi-modal axial-flexural waves (i.e. Lamb waves) [59]. The symmetric Lamb waves (S0 mode) have a large in-plane (axial) component of wave motion and antisymmetric Lamb waves (A0 mode) have a large out-of-plane (flexural) component of wave motion [60]. Both in-plane, as well as out-of-plane wave modes, are present at broad frequency range. Usually, at lower frequencies, A0 Lamb wave mode has a higher amplitude than S0 mode. For higher frequencies, it is opposite.

From the above discussions, we may conclude that the AE waves propagated as both symmetric and antisymmetric Lamb waves in the specimen. The low-frequency antisymmetric Lamb waves which had mostly the out-plane wave motion were captured by both PWAS and S9225. But, the high-frequency symmetric Lamb waves were captured by the PWAS only. Since the S9225 was not sensitive enough to capture the axial wave modes, it was not able to capture the higher frequency symmetric Lamb wave modes.

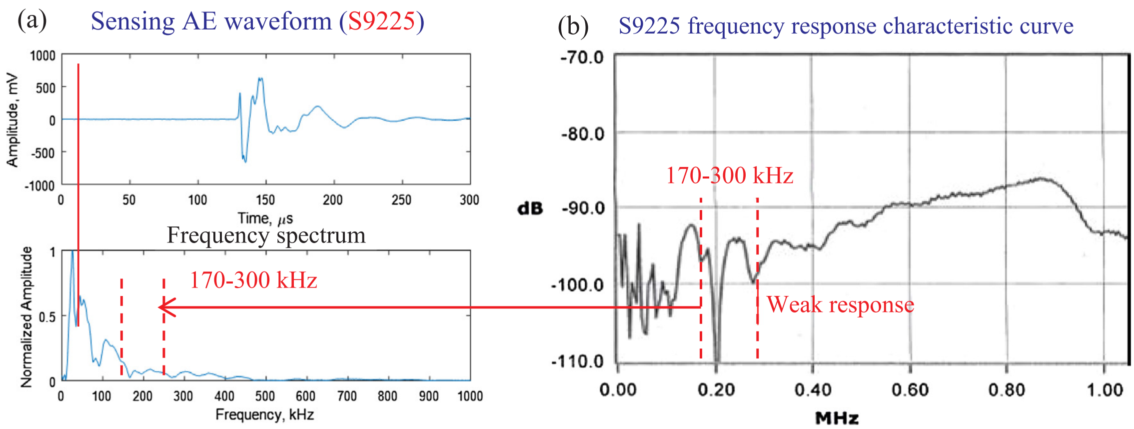

Fig. 14. (a) A typical sensing AE waveform and its frequency spectrum captured by the S9225, (b) the frequency response characteristic curve of S9225 (obtained from the manufacturer [20]); it showed a weak response in the frequency range of 170–300 kHz; the S9225 also sensed a weak signal in this range.

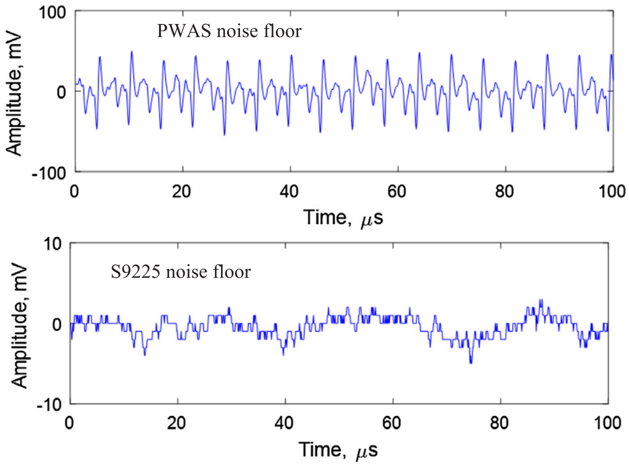

Fig. 15. Noise floor of PWAS and S9225 sensor.

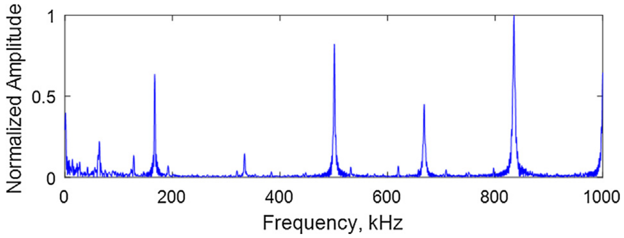

Fig. 16. Harmonic frequencies of the noise floor of PWAS.

4.5. Noise floor analysis of the sensors

This section compares the noise floor of the PWAS and S9225 sensors and explains the noise floor reduction for PWAS.

4.5.1. Noise floor comparison of PWAS and S9225

Fig. 15 shows the noise floor of PWAS and S9225 which have been observed during the AE-fatigue experiments. It can be observed that PWAS has more noise than the S9225. This may be because S9225 has better electromagnetic interference (EMI) shielding than PWAS. This noise has a regular periodic pattern in the time domain.

The harmonic frequencies of the PWAS noise are shown in Fig. 16. It shows that the noise has higher harmonics of about 167-kHz frequencies and very sharp amplitude peaks at these frequencies.

4.5.2. Noise floor reduction from the PWAS sensor

Although PWAS has a higher noise floor, they can easily be minimized. There are two ways to reduce the noise floor of PWAS as adopted in this research. They are: (1) using a coaxial cable with a minimum exposure of connecting-wire (Fig. 17), (2) a “noise cancellation” based signal processing. The detail of the noise cancellation has not been given for the sake of brevity. The readers may find the background of noise cancellation based denoising in Ref. [61].

Fig. 18 shows that the noise floor of PWAS has been significantly

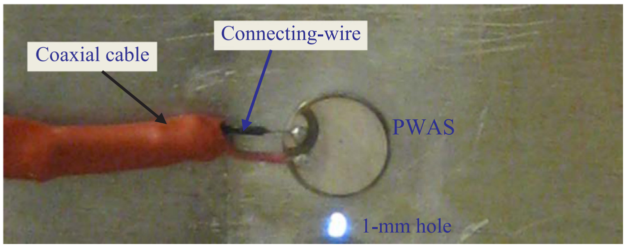

Fig. 17. PWAS with an attached coaxial cable with a minimum exposure of connecting-wire. (For scale, please note, the hole has 1-mm diameter).

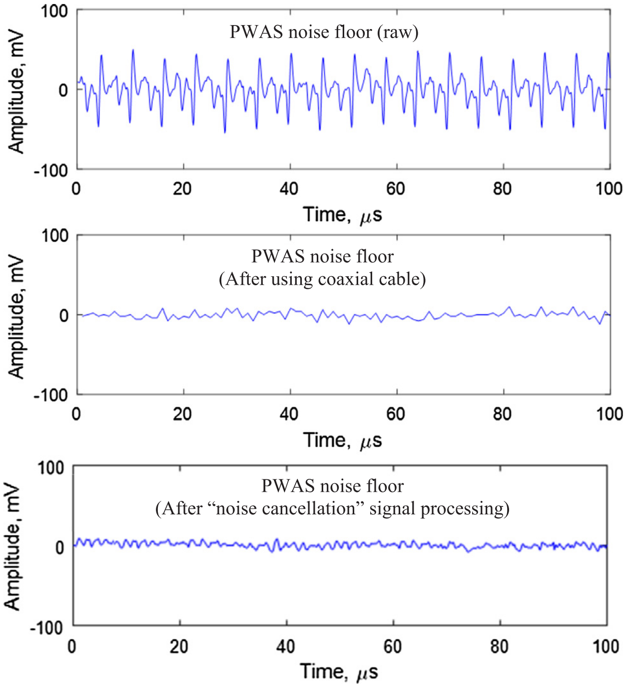

Fig. 18. Noise floor reduction from the PWAS.

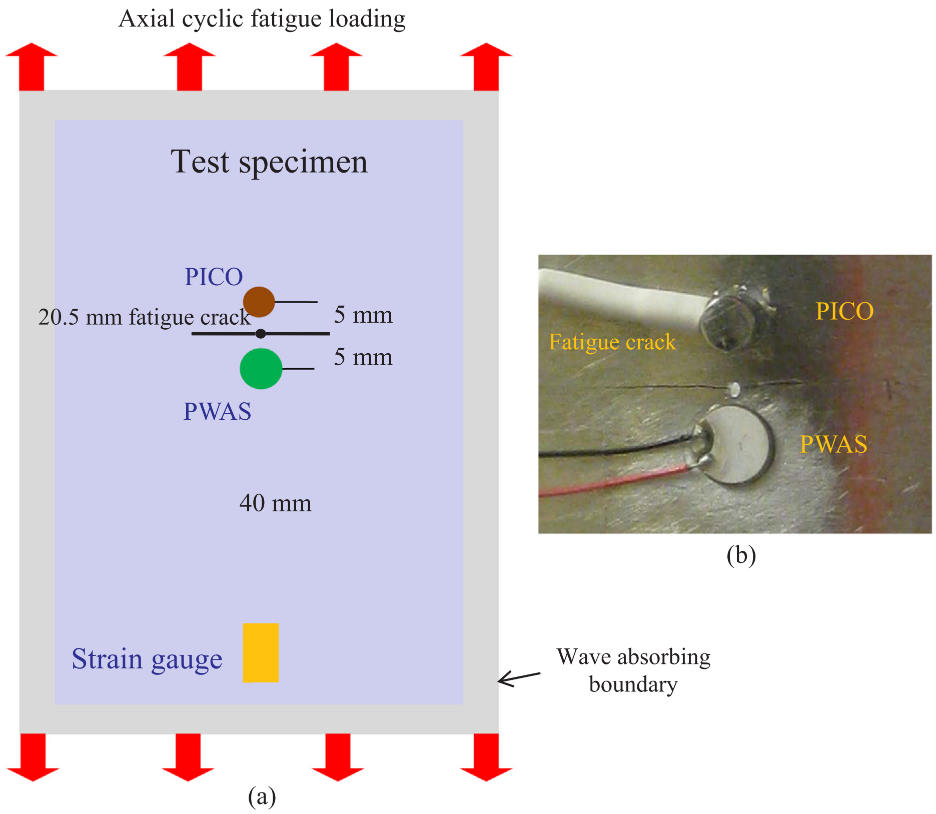

Fig. 19. (a) Schematic diagram of the experimental setup with PWAS and PICO AE sensors. The two sensors were symmetrically bonded at 5-mm from the crack, on the same side of the specimen. (b) A zoomed-in view of the PWAS and PICO with respect to the fatigue crack. For scale, please note, the hole has 1-mm diameter.

minimized by using the above-mentioned methods. Also, it can be noted that some AE signals are so strong (as shown in Figs. 11 and 12) that the noise floor is well below the signal strength. In appropriate cases, these denoising techniques may be implemented to obtain the cleaner AE signals and reveal their frequency content related to fatigue cracking as contained in the AE waveform.

5. AE-fatigue experiment with PWAS and PICO sensors

We performed an in-situ AE-fatigue experiment on the same specimen with another type of AE sensor (model PICO from PAC MISTRAS Inc.) along with PWAS. The experimental parameters were kept same as the previous one and the description of the experiment will not be repeated. The schematic of the test specimen with PWAS and PICO sensor is shown in Fig. 19a.

The relative position of the PWAS and PICO on the actual specimen is shown in Fig. 19b. Both of them are bonded at 5-mm from the fatigue crack. The diameter of the PWAS was 7-mm and the diameter of the PICO was 4.75-mm. the thickness of the PWAS was 0.5-mm. For PICO, the threshold was set to 2 dB above its noise level (41 dB).

5.1. Similarity between PWAS vs PICO

The AE hit-based analysis shows a similar pattern in PWAS and S9225 results. The AE hits were captured by the PWAS and PICO AE sensors as the fatigue crack grew. A source localization method was performed to verify that fatigue crack was the source of these AE hits and reported in our recent communication [17]. The AE hits captured by the PWAS and PICO for 50 fatigue cycles are shown in Fig. 20. In this particular 50 fatigue cycles, crack growth was optically measured as 300-µm. The average crack growth can be calculated as 6-µm/cycle.

In Fig. 20, both PWAS and PICO show a similar pattern in the hit-amplitude. In PWAS AE hit plot, there are higher-amplitude AE hits of almost constant amplitude of 96 dB. There are densely populated AE hits of variable amplitudes between 57 and 78 dB. Similarly, in PICO AE hit plot, there are higher-amplitude AE hits of almost constant amplitude of 96 dB. There are densely populated AE hits of variable amplitudes between 45 and 63 dB.

It can be noted that PICO AE hit amplitudes were higher than that of the S9225. This may be because the size of the PICO (4.75 mm diameter) was larger than the size of the S9225 (3.5 mm diameter) AE sensor. The PWAS hit amplitudes were higher than that of the PICO. This may be because the size of PWAS was larger than PICO. Also, they had different piezoelectric transduction factors, and sensing mechanisms. In this particular 50 cycles, PWAS captured 427 AE hits while the PICO captured 305 AE hits because some of the low-amplitude AE hits fall below the threshold setting of PICO. Except these very low-amplitude AE hits, both of them successfully captured the fatigue crack generated AE events.

The PWAS and PICO AE hits and the fatigue loading were plotted in a common timeline as shown in Fig. 21. Only 10 fatigue cycles' results are shown in this Figure to maintain the clarity of AE hit variation with fatigue loading. It shows that the multiple AE hits happened at every cycle. At a particular instant, a pair of AE hits can be observed: one captured by PWAS (marked by blue "square"), other captured by PICO (marked by red "diamond"). This indicated that they captured the same AE event at almost same time. The AE hits occurred during the cyclic loading period (from minimum load to maximum load) only. In the unloading period (from maximum load to minimum load), no AE hits were observed.

The AE hits started appearing at 53% of the maximum load level and continued until 84% of the maximum load level at some intervals. So far the PWAS and PICO showed the very similar pattern from the AE-hit based analysis. Both of them captured the fatigue crack generated AE hits with the very similar level of detail.

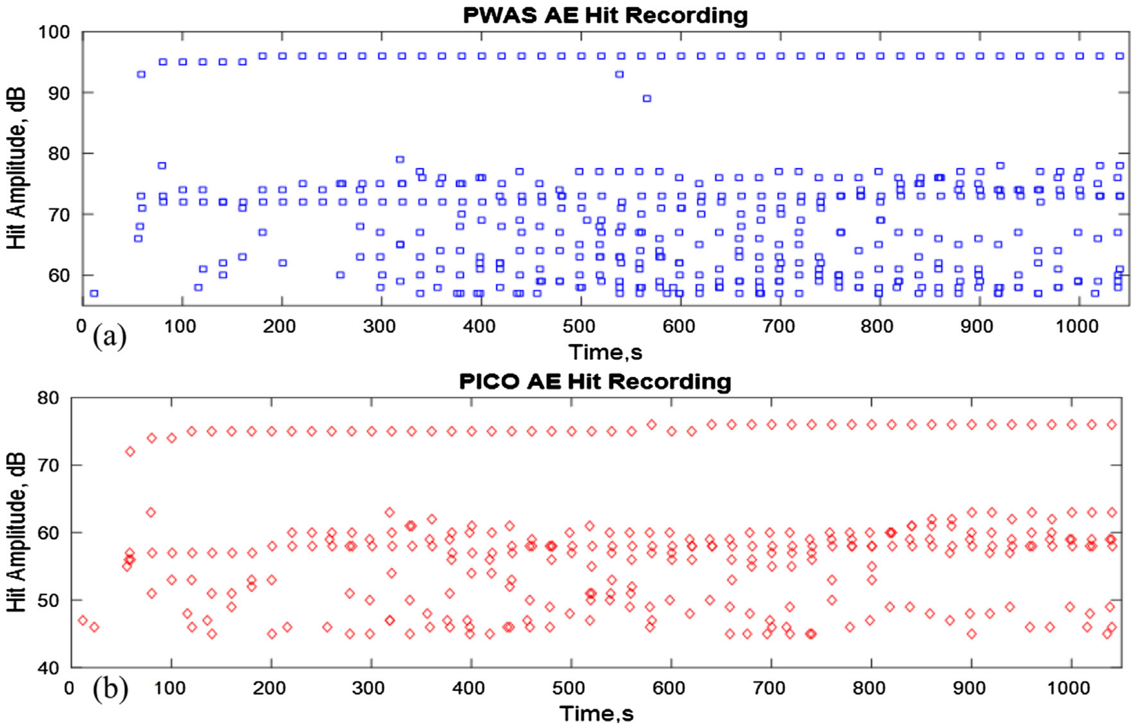

Fig. 20. The AE hits captured by the PWAS and PICO AE sensors. Both of them showing a similar trend in the AE-hit plots: the higher-amplitude AE hits on the top with a densely populated lowe-amplitude AE-hits on the bottom. In these plots, PWAS has 427 hits and S9225 has 305 hits.

5.2. AE waveform-based analysis for PWAS and PICO results

PWAS and PICO AE sensors were compared based on the AE waveforms and their frequency spectra. It was found that all the PWAS and PICO AE waveforms were different even though the AE hits from the same AE event were compared. Three pairs of AE hits as marked by “1”, “2”, “3” on Fig. 21 were considered for comparison. Pairs “1” and “2” are the representatives of all the higher amplitude AE hits. Pair “3” is the representative of the lower amplitude AE hits.

The PWAS and PICO AE waveforms for a particular AE event that happened at 360.36 s (“1”) are shown in Fig. 22a and b. The AE hits corresponding to this AE event belong to the higher amplitude AE hits (group B) of the previous 60 cycle result as discussed in the earlier section. The PWAS captured the AE waveform that was consistent with the previous 60 fatigue cycle result. But the PICO waveform (Fig. 22a) was different from the S9225 waveform (Fig. 12b) even though they had the same mechanism of sensing. The PICO waveform contained a ringing noise.

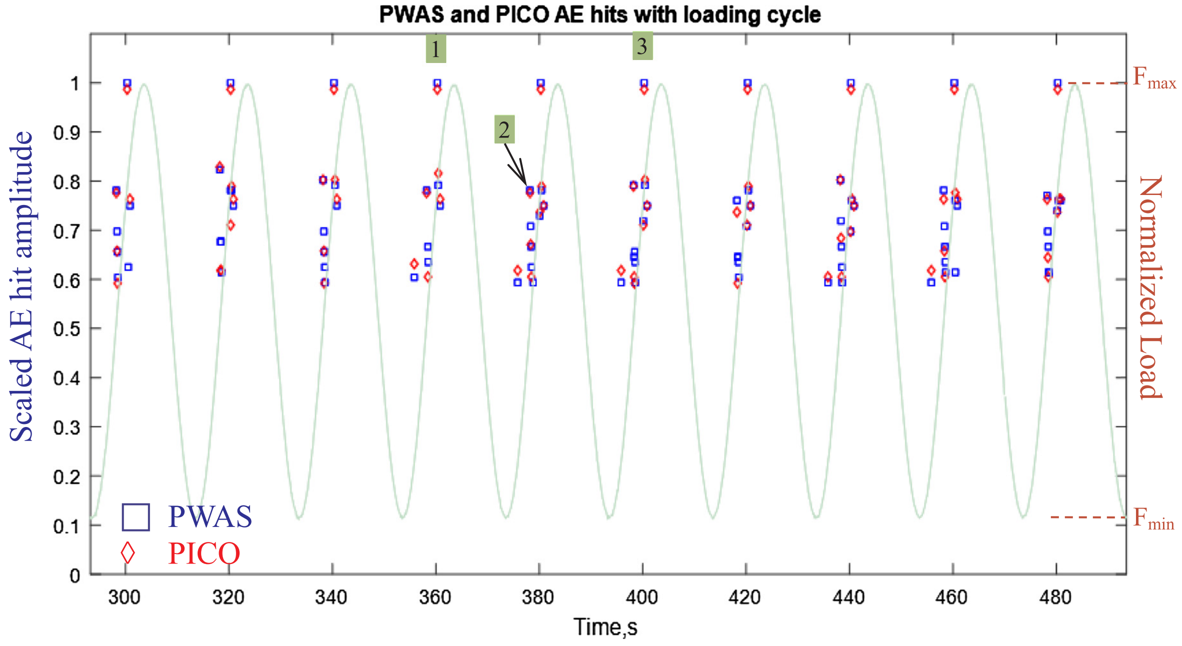

Fig. 21. PWAS and PICO AE hits synchronized with the fatigue loading cycle. Both of them captured the AE hits on the loading part (on the way from F_{min} to F_{max}) of the cycle. On the unloading side, no AE hits were observed. Please note, the PWAS AE hits are marked by “square” and the PICO AE hits are marked by “diamond” markers.

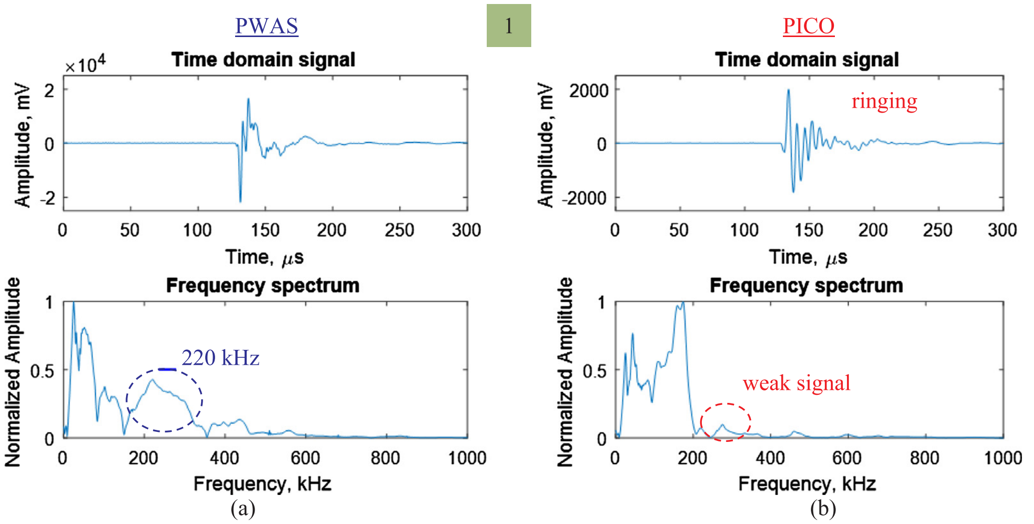

(a) (b)

Fig. 22. The comparison between PWAS and PICO AE waveforms and their frequency spectra for the same AE event at approx. 360.36 s (marked by “1” in Fig. 21). Both of them captured the frequencies until 200-kHz. The PICO has the “ringing” waveform. The PWAS captured low-frequency contents plus 220-kHz, 450-kHz frequency peaks.

The frequency spectra of the PWAS and PICO are also illustrated in Fig. 22a and b. It shows that the low-frequency peaks such as 30, 60, 110 kHz are captured by both PWAS and PICO AE sensors. But, the PICO had the highest peak at 170-kHz and there was a sudden drop in the frequency spectrum after 170-kHz. On the other hand, PWAS captured the 220-kHz and 450-kHz frequency peaks. The PICO showed a very weak response at these frequencies.

The time-domain waveforms and frequency spectra captured by PWAS and PICO are shown in Fig. 23a and b. These waveforms are corresponding to the pair of AE hits that are captured at 378.79 s (marked by “2” in Fig. 21). The frequency spectra show that the low-frequency peaks are somewhat similar in both PWAS and PICO AE sensors. But, the PICO had the highest peak at 170-kHz and there was a sudden drop in the frequency spectrum after 170-kHz. The PWAS captured a wideband frequency of 110–300 kHz. The PICO showed a very weak response after 200-kHz. The PICO waveform also contained a ringing noise.

The PWAS and PICO AE waveforms corresponding to the AE hits at 400.36 s (“3”) have shown the similar differences in the frequency spectra as in “1” and is not repeated. Hence, the acoustic emissions captured by the PWAS and PICO showed a significant difference based on the AE waveform analysis.

5.3. Possible explanation for weak response of PICO

PICO was showing some weak response at some higher frequency peaks. A typical PICO sensing signal and its frequency spectrum are shown in Fig. 24a. The frequency response characteristic plot collected from the sensor manufacturer is shown in Fig. 24b. The frequency characteristic plot shows a peak frequency at 170-kHz. This explained why the frequency spectrum of the sensing signal showed a peak frequency of 170-kHz. Also, the PICO frequency characteristic plot shows a weak response at 180–270 kHz band. Thus it showed a weak response at 180–270 kHz band in the sensing signal (Fig. 24a).

The PICO was also showing the weak response for higher frequencies such as 300, 450-kHz. This may be because of the sensing mechanism of the PICO sensor. The PICO sensor was sensitive to the out-of-plane wave motion. The symmetric Lamb wave modes have predominantly in-plane wave motion and a very weak out-of-plane component of wave displacement. This may explain why PICO was showing a weak response at these frequencies (300 and 450-kHz).

In both experiments, the PWAS and the commercial AE sensors (S9225 and PICO) showed a very similar pattern from the AE hit based analysis. But they showed significant differences from the AE-waveform based analysis. In both cases, PWAS showed higher signal-to-noise in the high-frequency region than that of the S9225 and PICO AE sensors.

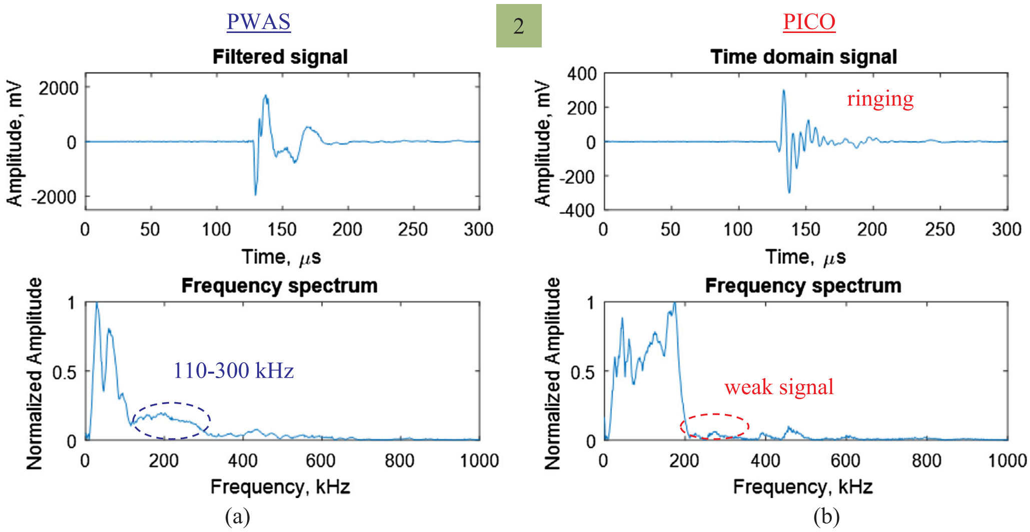

(a) (b)

Fig. 23. The comparison between PWAS and PICO AE waveforms and their frequency spectra for the same AE event at approx. 378.79 s (marked by “2” in Fig. 21). Both of them captured the frequencies until 200-kHz. The PICO has the “ringing” waveform. The PWAS captured a wideband (110–300 kHz) frequencies.

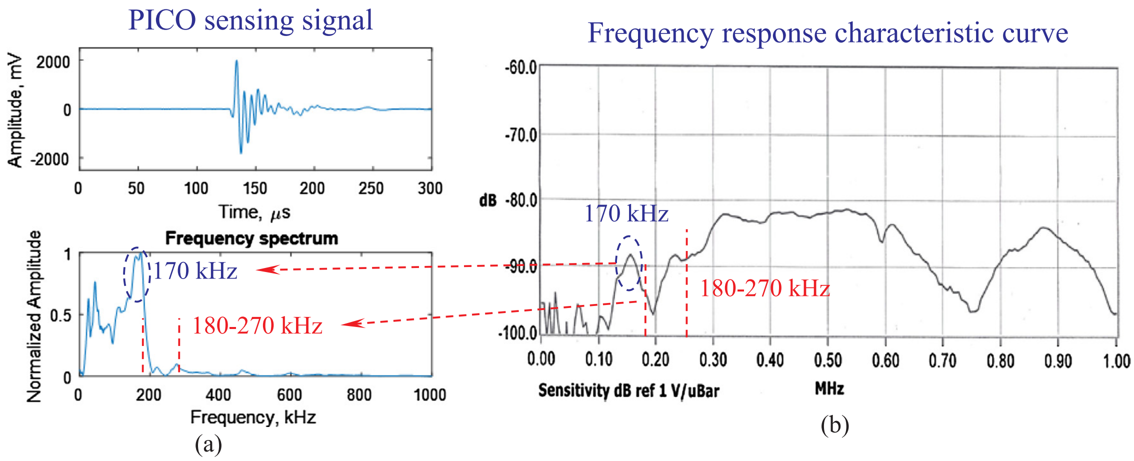

(a) (b)

Fig. 24. (a) A typical AE waveform and its frequency spectrum captured by the PICO AE sensor, (b) the frequency response characteristic curve of PICO (obtained from the manufacturer); it showed a peak at 170-kHz and the sensing signal also showed a peak response at 170-kHz. The characteristic plot showed a weak response in the frequency range of 180–270 kHz; the PICO also sensed a weak signal in this range.

6. Conclusion

Piezoelectric wafer active sensor (PWAS) successfully captured the acoustic emissions generated by the fatigue crack. PWAS, S9225, and PICO show a very similar pattern of the AE hits. It has been shown that the AE sensor type has a significant effect on the captured AE waveform and its frequency spectrum. We found that a certain sensor may be more suitable than others depending on the application. The PWAS shows a better signal-to-noise ratio in the high-frequency region than the commercial AE sensor (PICO and S9225). The AE hit-based analysis may not be sufficient to understand the fatigue crack generated AE signals. The AE waveform-based analysis gives much more insight detail of the AE source than that of the AE-hit based analysis. As the AE signals propagate in the thin plate as guided waves, it was found that both axial (symmetric) and flexural modes (antisymmetric) of Lamb waves may be present in the AE wave propagation. The out-of-plane sensitive sensors (like S9225 and PICO) measure the low-frequency flexural modes. But they show a very weak response to the axial (symmetric) modes. The PWAS captures both axial and flexural modes of the Lamb waves due to acoustic wave propagation. Thus, PWAS can be used as an AE sensor for monitoring the fatigue crack in the thin plate-like structures.

7. Future work

The PWAS AE waveforms would be further analyzed from to find any possible correlation with the fatigue crack length. Any waveform group other than group A, B (as discussed in the article) may be searched for in order to find any potential relationship between the fatigue crack lengths. The mechanism of crack growth within one fatigue cycle may be established from the captured AE signals. In-situ microscopic measurement of the fatigue crack length would be performed and correlated with the captured AE signals.

Acknowledgment

Support of Office of Naval Research, the U.S. Navy, #N00014-14-1-0655, Dr. Ignacio Perez, Program Manager is thankfully acknowledged.

Appendix A. Supplementary material

Supplementary data associated with this article can be found, in the online version, at https://doi.org/10.1016/j.ultras.2018.08.020.

References

[1] S. Yin, Z. Cui, T. Kundu, Acoustic source localization in anisotropic plates with 'Z' shaped sensor clusters, Ultrasonics 84 (2018) 34–37.
[2] K. Wang, M. Liu, Z. Su, S. Yuan, Z. Fan, Analytical insight into 'breathing' crack-induced acoustic nonlinearity with an application to quantitative evaluation of contact cracks, Ultrasonics 88 (2018) 157–167.
[3] S. Chen, C. Yang, G. Wang, W. Liu, Similarity assessment of acoustic emission signals and its application in source localization, Ultrasonics 75 (2017) 36–45.
[4] N. Favretto-Cristini, L. Hégron, P. Sornay, Identification of the fragmentation of brittle particles during compaction process by the acoustic emission technique, Ultrasonics 67 (2016) 178–189.
[5] M.Y. Bhuiyan, J. Bao, B. Poddar, V. Giurgiutiu, Analysis of acoustic emission waveforms from fatigue cracks, in: SPIE Proceedings of Health Monitoring of Structural and Biological Systems, vol. 10170, 2017, p. 101702A–1–8.
[6] T.C. Lindley, I.G. Palmer, C.E. Richards, Acoustic emission monitoring of fatigue crack growth, Mater. Sci. Eng. 32 (1978) 1–15.
[7] F. Hamel, J.P. Bailon, M.N. Bassim, Acoustic emission mechanisms during high-cycle fatigue, Eng. Fract. Mech. 14 (4) (Jan. 1981) 853–860.
[8] C.B. Scruby, G.R. Baldwin, K.A. Stacey, Characterization of fatigue crack extension by quantitative acoustic emission, Int. J. Fract. 28 (1985) 201–222.
[9] M.N. Bassim, Detection of fatigue crack propagation with acoustic emission, NDT&E Int. 25 (6) (1992) 287–289.
[10] J.J. Lucas, Acoustic Emission Fatigue Crack Monitoring of a Simulated Aircraft Fuselage Structure, Embry-Riddle Aeronautical University, 2010.
[11] C. Chen, W. Sachse, Quantitative acoustic emission source characterization of fatigue cracks in a thin-plate of 7075–T6 aluminum, J. Appl. Phys. 64 (11) (1988) 6264–6273.
[12] A. Berkovits, D. Fang, Study of fatigue crack characteristics by acoustic emission, Eng. Fract. Mech. 51 (3) (1995) 401–416.
[13] A.K. Maji, D. Satpathi, T. Kratochvil, Acoustic emission source location using lamb wave modes, J. Eng. Mech. 123 (2) (Feb. 1997) 154–161.
[14] J. Jingpin, W. Bin, H. Cunfu, Acoustic emission source location methods using mode and frequency analysis, Struct. Control Heal. Monit. 15 (4) (2008) 642–651.
[15]] M.Y. Bhuiyan, J. Bao, B. Poddar, V. Giurgiutiu, Toward identifying crack-length-related resonances in acoustic emission waveforms for structural health monitoring applications, Struct. Heal. Monit. Int. J. (2017) 1–9.
[16] D. Gagar, P. Foote, P. Irving, A novel closure based approach for fatigue crack length estimation using the acoustic emission technique in structural health monitoring applications, Smart Mater. Struct. 23 (10) (2014) 105033.
[17] M.Y. Bhuiyan, V. Giurgiutiu, The signatures of acoustic emission waveforms from fatigue crack advancing in thin metallic plates, Smart Mater. Struct. 27 (1) (2017) 1–15.
[18] J.A. Simmons, C.D. Turner, H.N.G. Wadley, Vector calibration of ultrasonic and acoustic emission transducers, J. Acoust. Soc. Am. 82 (4) (1987) 1122–1130.
[19] A. Ghoshal, W.H. Prosser, B.M. Copeland, Development of piezoelectric acoustic sensors and novel bio-inspired sensor array architecture, AIP Conf. Proc. 700 (1) (2004) 737–744.
[20] Complete Line of Standard Acoustic Emission Sensors, PAC MISTRAS Inc., 2016.
[21] D. Adams, Health Monitoring of Structural Materials and Components: Methods with Applications, Wiley, 2007.
[22] A.A. Pollock, Acoustic emission inspections, 1989.
[23] R.K. Miller, E.K. Hill, P.O. Moore, Nondestructive Testing Handbook: Acoustic Emission Testing, third ed., American Society for Nondestructive Testing, Columbus, OH, USA, 2005.
[24] P.V. Abraham, et al., An integrated structural health monitoring approach for crack growth monitoring, J. Intell. Mater. Syst. Struct. 23 (14) (2012) 1563–1573.
[25] R.V. Sagar, B.K.R. Prasad, A review of recent developments in parametric based

acoustic emission techniques applied to concrete structures, Nondestruct. Test. Eval. 27 (1) (2012) 47–68.
[26] P.D. Theobald, T.J. Esward, S.P. Dowson, R.C. Preston, Acoustic emission transducers—development of a facility for traceable out-of-plane displacement calibration, Ultrasonics 43 (5) (2005) 343–350.
[27] T. Kishi, M. Ohtsu, S. Yuyama, Acoustic Emission - Beyond the Millennium, Elsevier, 2000.
[28] W.H. Prosser, M.A. Hamstad, J. Gary, A. O'Gallagher, Finite element and plate theory modeling of acoustic emission waveforms, J. Nondestruct. Eval. 18 (3) (1999) 83–90.
[29] K.Y. Kim, W. Sache, Characteristics of an acoustic emission source from a thermal crack in glass, Int. J. Fract. 31 (3) (1986) 211–231.
[30] D. Li, Z. Chen, Q. Feng, Y. Wang, Damage analysis of CFRP-confined circular concrete-filled steel tubular columns by acoustic emission techniques, Smart Mater. Struct. 24 (8) (2015) 085017.
[31] M.G.R. Sause, S. Richler, Finite element modelling of cracks as acoustic emission sources, J. Nondestruct. Eval. 34 (1) (2015) 4.
[32] A.A. Abouhussien, A.A.A. Hassan, Detection of bond failure in the anchorage zone of reinforced concrete beams via acoustic emission monitoring, Smart Mater. Struct. 25 (7) (2016) 075034.
[33] A. Ebrahimkhanlou, B. Dubuc, S. Salamone, A guided ultrasonic imaging approach in isotropic plate structures using edge reflections, in: SPIE Smart Structures and Materials, Nondestructive Evaluation and Health Monitoring, vol. 9803, 2016, p. 98033I–9803–8.
[34] A. Baghalian, S. Tashakori, V.Y. Senyurek, D. McDaniel, H. Fekrmandi, I.N. Tansel, Non-contact quantification of longitudinal and circumferential defects in pipes using the surface response to excitation (sure) method, Int. J. Progn. Heal. Manage. 8 (2) (2017) 1–8.
[35] E. Verstrynge, H. Pfeiffer, M. Wevers, A novel technique for acoustic emission monitoring in civil structures with global fiber optic sensors, Smart Mater. Struct. 23 (6) (2014) 65022.
[36] R. Ernst, F. Zwimpfer, J. Dual, One sensor acoustic emission localization in plates, Ultrasonics 64 (2016) 139–150.
[37] I.M. Perez, H. Cui, E. Udd, Acoustic emission detection using fiber Bragg gratings, in: SPIE's 8th Annu. Int. Symp. Smart Struct. Mater., vol. 4328, 2001, pp. 209–215.
[38] C. Zhou, Y. Zhang, Acoustic emission source localization using coupled piezoelectric film strain sensors, J. Intell. Mater. Syst. Struct. 25 (16) (2014) 2082–2092.
[39] M.J. Sundaresan, A. Ghoshal, W.N. Martin, M.J. Schulz, A continuous sensor to measure acoustic waves in plates, J. Intell. Mater. Syst. Struct. 12 (1) (2001) 41–56.
[40] Q. Xie, X. Liu, J. Tao, T. Li, S. Cheng, F. Lu, Experimental verification of the sparse design of a square partial discharge acoustic emission array sensor, Meas. Sci. Technol. 26 (4) (2015) 45101.
[41] B. Saha, et al., Acoustic emission and changes in dislocation structure and magnetostriction accompanying plastic deformation of [126]-oriented Fe-Ga alloy single crystals, J. Appl. Phys. 114 (22) (2013) 223910.
[42] H. Chang, E.H. Han, J.Q. Wang, W. Ke, Acoustic emission study of fatigue crack closure of physical short and long cracks for aluminum alloy LY12CZ, Int. J. Fatigue 31 (3) (2009) 403–407.
[43] T.M. Roberts, M. Talebzadeh, Acoustic emission monitoring of fatigue crack propagation, J. Constr. Steel Res. 59 (6) (2003) 695–712.
[44] O. Andreykiv, V. Skalsky, O. Serhiyenko, D. Rudavskyy, Acoustic emission estimation of crack formation in aluminium alloys, Eng. Fract. Mech. 77 (5) (2010) 759–767.
[45] C.K. Lee, P.D. Wilcox, B.W. Drinkwater, J.J. Scholey, M.R. Wisnom, M.I. Friswell, Acoustic emission during fatigue crack growth in aluminium plates, in: Proc. ECNDT, vol. Mo.2.1.5, 2006, pp. 1–8.
[46] T.M. Morton, R.M. Harrington, J.G. Bjeletich, Acoustic emissions of fatigue crack growth, Eng. Fract. Mech. 5 (3) (1973) 691–697.
[47] K. Nam, A. Mal, Characteristics of elastic waves generated by crack initiation in aluminum alloys under fatigue loading, J. Mater. Res. 16 (6) (2001) 1745–1751.
[48] A. Ould Amer, A.L. Gloanec, S. Courtin, C. Touze, Characterization of fatigue damage in 304L steel by an acoustic emission method, Procedia Eng. 66 (2013) 651–660.
[49] L. Yu, G. Santoni-Bottai, B. Xu, W. Liu, V. Giurgiutiu, Piezoelectric wafer active sensors for in situ ultrasonic-guided wave SHM, Fatigue Fract. Eng. Mater. Struct. 31 (8) (2008) 611–628.
[50] L. Yu, S. Momeni, V. Godinez, V. Giurgiutiu, Adaptation of PWAS transducers to acoustic emission sensors, in: Proceedings of SPIE , Nondestructive Characterization for Composite Materials, Aerospace Engineering, Civil Infrastructure, and Homeland Security, vol. 7983, 2011, pp. 798310–798327.
[51] C. Zhou, M. Hong, Z. Su, Q. Wang, L. Cheng, Evaluation of fatigue cracks using nonlinearities of acousto-ultrasonic waves acquired by an active sensor network, Smart Mater. Struct. 22 (1) (2013) 15018.
[52] M.Y. Bhuiyan, Y. Shen, V. Giurgiutiu, Guided wave based crack detection in the rivet hole using global analytical with local FEM approach, Materials (Basel) 9 (7) (2016) 602.
[53] S.C. Stanton, A. Erturk, B.P. Mann, D.J. Inman, Nonlinear piezoelectricity in electroelastic energy harvesters: modeling and experimental identification, J. Appl. Phys. 108 (7) (2010) 74903.
[54] M.Y. Bhuiyan, V. Giurgiutiu, Multiphysics simulation of low-amplitude acoustic wave detection by piezoelectric wafer active sensors validated by in-situ AE-fatigue experiment, Materials (Basel) 10 (8) (2017) 1–19.
[55] M.R. Gorman, W.H. Prosser, Application of normal mode expansion to acoustic emission waves in finite plates, J. Appl. Mech. 63 (2) (1996) 555–557.
[56] Mistras Group - Acoustic Emission Services.
[57] V. Giurgiutiu, Structural Health Monitoring with Piezoelectric Wafer Active Sensors, second ed., Academic Press, Oxford, 2014.
[58] Steiner & Martins, Inc., USA.
[59] V. Giurgiutiu, Lamb-wave embedded NDE with piezoelectric wafer active sensors for structural health monitoring of thin-wall structures, AIP Conf. Proc. 700 (1) (2004) 1452–1459.
[60] Y. Lu, L. Ye, Z. Su, Crack identification in aluminium plates using Lamb wave signals of a PZT sensor network, Smart Mater. Struct. 15 (3) (2006) 839.
[61] K.S.C. Kuang, D. Li, C.G. Koh, Acoustic emission source location and noise cancellation for crack detection in rail head, Smart Struct. Syst. 18 (5) (2016) 1063–1085.